Combined Au/Ag nanoparticle creation in ZnO nanopillars by ion implantation for optical response modulation and photocatalysis

A. Macková[*ab], A. Jagerová[ab], O. Lalik[ab], R. Mikšová[a], D. Poustka[c] , J. Mistrík[de], V. Holý[fg], J. D. Schutter[h], U. Kentsch[i], P. Marvan[j], A. Azarov[k], A. Galeckas[k]

[a] *Nuclear Physics Institute of the Czech Academy of Sciences, v. v. i., 250 68 Řež, Czech Republic*

[b] *Department of Physics, Faculty of Science, J. E. Purkinje University, Pasteurova 3544/1, 400 96 Ústí nad Labem, Czech Republic*

[c] *Centre for Nanomaterials and Biotechnology, Faculty of Science, J. E. Purkinje University, Pasteurova 3544/1, 400 96 Ústí nad Labem, Czech Republic*

[d] *Institute of Applied Physics and Mathematics, Faculty of Chemical Technology, University of Pardubice, 532 10 Pardubice, Czech Republic*

[e] *Centre of Materials and Nanotechnologies, Faculty of Chemical Technology, University of Pardubice, 530 02 Pardubice, Czech Republic*

[f] *Department of Condensed Matter, Faculty of Mathematics and Physics, Charles University, Ke Karlovu 2026/5, 121 16 Prague 2, Czech Republic*

[g] *Faculty of Science, Masaryk University, Kotlářská 2, 61137 Brno, Czech Republic*

[h] *Bundesanstalt für Materialforschung und -prüfung (BAM), Unter den Eichen 87, 12205, Berlin, Germany*[i]*Helmholtz-Zentrum Dresden-Rossendorf, Institute of Ion Beam Physics and Materials Research, Bautzner Landstraße 400, 01328, Dresden, Germany*

[j] *Department of Inorganic Chemistry, University of Chemistry and Technology, 166 28 Prague, Czech Republic*

[k] *Department of Physics, Centre for Materials Science and Nanotechnology, University of Oslo, P.O. Box 1048, Blindern, N-0316 Oslo, Norway*

**corresponding author: mackova@ujf.cas.cz*

Abstract

ZnO nanopillars were implanted with Au-400keV and Ag-252keV ions with ion fluences from 1 × 10^{15} cm^{-2} to 1 × 10^{16} cm^{-2}. We compared ZnO nanopillars solely implanted with Au-ions and dually-implanted with Au and Ag-ions. Rutherford Back-Scattering spectrometry (RBS) confirmed Ag and Au embedded in ZnO nanopillar layers in a reasonable agreement with theoretical calculations. A decreasing thickness of the ZnO nanopillar layer was evidenced with the increasing ion implantation fluences. Spectroscopic Ellipsometry (SE) showed a decrease of refractive index in the nanopillar parts with embedded Au, Ag-ions. XRD discovered vertical domain size decreasing with the proceeding radiation damage accumulated in ZnO nanopillars which effect was preferably ascribed to Au-ions. SE and diffuse reflectance spectroscopy (DRS) showed optical activity of the created nanoparticles at wavelength range 500 – 600 nm and 430 – 700 nm for the Au-implanted and Au, Ag-implanted ZnO nanopillars, respectively. Photoluminescence (PL) features linked to ZnO deep level emission appear substantially enhanced due to plasmonic interaction with metal nanoparticles created by Ag, Au-implantation. Photocatalytic activity seems to be more influenced by the nanoparticles presented in the layer rather than the surface morphology. Dual implantation with Ag, Au-ions enhanced optical

activity to a larger extent without significant morphology deterioration as compared to the solely Au-ion implanted nanopillars.

Keywords
ZnO nanopillars; Au/Ag nanoparticles, ion implantation; SPR; doped ZnO nanostructures

1. Introduction

Ion implantation of metals into ZnO nanostructures offers a promising way for creating bi-metallic Ag/Au nanoparticles. Metal ion-implantation and irradiation with adjustable ion energy and fluence facilitate formation of enriched layer at appropriate depth of solid matter which can lead to metal nanoparticle (NP) creation; furthermore, such an approach also allows to realize intentional defect aggregation via high energy transfer of highly energetic ions [1, 2]. These processes are able to modify optical properties of ion-irradiated nanostructures and distinct new phenomena can appear in comparison with bulk materials. Due to ZnO wide bandgap energy (3.37 eV), large free exciton energy (60 meV) and high luminescence efficiency [3, 4], doping of ZnO nanostructures with Ag, Au and bi-metallic Ag/Au NPs has become very attractive and challenging for the preparation of nano-optics devices. Recently, such structures were prepared and investigated as DNA sensor and for biological applications in general [5-7]. ZnO forms a large variety of nanostructures, e.g., nanorods, nanowires, nanodots, etc., whose optical properties have been very intensively investigated [8]. The high surface-to-volume ratio of ZnO nanowires accompanied by efficient electron-hole pair generation under UV irradiation ensure the high sensitivity of UV detectors [9-11]. The sensitivity and fast response of ZnO optoelectronics can be further enhanced by Au and Ag-NPs exhibiting surface plasmon resonance (SPR) activity [12,13]. By using more than one metal, special properties can be obtained due to the synergetic effect between used atoms which can overcome some limitations of monometallic-NPs. For instance, the bimetallic Au/Ag NPs potentially offer SPR optical activity that can be tuned in a wide range of wavelengths starting from 400 nm (typical for Ag-NPs) up to 550 nm (for Au-NPs) depending on their composition and size.

Furthermore, combining the high coalescence ability of Au-atoms and Ag reactivity with oxygen can be used for the preparation of highly stable NPs with enhanced photocatalytic properties. ZnO is a common starting material in applications for photocatalytic degradation of organic molecules, sensor and biosensor construction. The photocatalytic degradation of various organic dyes was studied for pristine [14] as well as ZnO nanorods modified with monometallic Au, Ag or Pt nanoparticles [15]. ZnO coatings with Au-NPs exhibited a higher response and faster time for recovery than pristine ZnO [16]. Bimetallic sub-sequential implantation was used for Au/Ag NPs preparation in amorphous silica glass [17, 18]; only a few studies focused on the preparation of bimetallic-NPs in a single-crystalline or poly-crystalline materials [19,20] or ZnO nanostructures. Polar *c*-plane ZnO substrates exhibit a quantum-confined Stark effect resulting in a decrease in device efficiency. Such effect can be compensated in non-polar crystallographic orientations, where Zn-cations and O-anions are equivalently positioned on the surface and form zero net dipole in the plane leading to the better efficiency of optoelectronic devices such as LED, detectors or sensors [21]. Radiation defects are formed in ZnO bulk after ion implantation, where significant connections between the dopant's chemical nature and defect have been discovered [22-24]. Damage accumulation and defect–dopant interaction in ZnO nanostructures will differ from the bulk ZnO, as the more crystallographic orientations are implanted/irradiated simultaneously during ion implantation [25]. Nanorods and nanowires of ZnO represent an exclusive

and sensitive system for analyzing ion implantation phenomena bringing un-expected changes in their properties. The relations of these phenomena are all crucial issues for the understanding of the complex ion interaction with ZnO nanopillars differing from bulk ZnO. Nanostructured ZnO would be more sensitive to dynamic annealing due to a high specific surface [25]. It has been shown, that heavy Ar-ion irradiation with energy 50 keV caused ZnO nanorod sharpening. Intentional nanoscale roughening (in nm scale) would be very prospective for specific catalytic applications [26], energetic ion beams have been successfully applied on nanograin ZnO layer, where controlled surface modification has been achieved [27]. Additionally, it is expected that surface defect engineering both influencing surface chemistry and potential applicability in sensing would be influenced as well.

Annealing treatment has to be chosen such a way, that it rather removes the implantation defects than deteriorates nanostructure quality. It has been reported recently, that short duration and low temperature during thermal treatment are preferable in order to not degrade the implanted ZnO nanorods [28-29]. It was demonstrated that increasing the time and temperature of annealing can be detrimental rather than beneficial. Due to results showing only slight internal structure recovery in ZnO nanopillars after the annealing at 750°C for 15 min [30], we didn't apply annealing on Au, Ag-ion dually implanted samples in this experiment. It is important to follow defect creation in nanostructures directly after the implantation. It was shown, that ZnO nanorods after irradiation by energetic Au ions in [25] that oxygen deficiency appeared on the nanorod surface. Dee et al. observed the transformation of ZnO nanowires from wurtzite structure into a disordered amorphous structure irradiated with 70 keV H^+ ions to ion fluences of 10^{17} ions.cm^{-2} due to the radiation defect accumulation and migration differing from a bulk, where such effect cannot be easily achieved at these conditions [31].

Optical properties of the Au-enriched layers can vary in dependence on ZnO facet due to the distinct internal morphology modification connected to radiation defect creation in various crystallographic orientations of ZnO [32, 33, 34]. This phenomenon is related to the role of radiation defect clustering, thermal stability and nature in different ZnO facets in connection to ion implantation [23, 31]. The photocatalytic application of ZnO nanostructures is a very topical research field nowadays, photocatalytic performances of ZnO are dependent on many factors, mainly the chemistry of nanorod surface, effective area or ZnO nanorods, their internal structure, the light source used for photocatalysis [35, 36].

Implantation sequence of the used Ag and Au-ions can influence the radiation defect accumulation and surface roughening of nanorods as well as clustering of two metals. In study by Peña *et al.* the authors have shown that Au/Ag core-shell NPs could be created in SiO_2 by keeping the implantation sequence of Ag first and Au ions second, whereas the reverse order led not to a core/shell (Ag/Au) NP but to NPs with an Au–Ag alloy [18].

Our experiments were motivated by the following issues: i) the structural and morphological modification of ZnO nanopillars after the Au/Ag-ion implantation, ii) Au/Ag incorporation and possible combined bi-metallic cluster formation in ZnO nanopillars, iii) optical absorption and emission (luminescence) properties of ZnO nanopillars with embedded Au and Ag ions in correlation to noble metal clustering and radiation defect accumulation, and iv) potential usability for photocatalytic degradation of organic dyes.

2. Experiment

2.1. ZnO nanopillar growth and Au/Ag ion implantation

ZnO nanopillars were grown on Si wafers using a hydrothermal approach [37]. The detailed description of the ZnO nanopillar deposition has been published also in [30]. ZnO nanopillars were implanted with the Au-400 keV and Ag-252keV ions using the fluence range of 1×10^{15} cm^{-2} - 1×10^{16} cm^{-2} using an implanter at the Ion Beam Center, HZDR Dresden-Rossendorf, Germany. The distinct ion energies were chosen due to the fact, that Ag-ions with lighter mass experienced lower energy stopping, thus the projected range is lower compared to Au-ions at the same energy. The Au/Ag-implantation was provided with inclining angle 7° to minimize implanted ion-penetration into the voids in ZnO nanopillar layer and to cumulate the maximal metal concentration in the upper part of the ZnO nanopillars.
The various combination of the Ag (implanted as first) and Au-ion (implanted as second) fluences were used to achieve the various Ag/Au ratios which can result in distinct metal distribution in the created NPs. The summarized Ag/Au ion implantation parameters are presented in **Table 1**.

Sample name/implantation type	Ion type	Ion energy (keV)	Ion implantation fluence (ions.cm^{-2})
S1/ sole Au-ion implantation	Au	400	1.0×10^{15}
S2/ sole Au-ion implantation	Au	400	5.0×10^{15}
S3/ sole Au-ion implantation	Au	400	10.0×10^{15}
S4/ dual Au+Ag - ion implantation	Ag	252	5.0×10^{15}
	Au	400	2.5×10^{15}
S5/ dual Au+Ag - ion implantation	Ag	252	5.0×10^{15}
	Au	400	5.0×10^{15}
S6/ dual Au+Ag - ion implantation	Ag	252	5.0×10^{15}
	Au	400	10.0×10^{15}

Table 1

Ion implantation parameters used for the ZnO nanopillar irradiation – implanted ion specie, ion energy and ion implantation fluence.

2.2. Structure and morphology analyses of ZnO nanopillars implanted with Au/Ag ions by XRD, RBS and SEM

X-ray diffraction (XRD) was used to follow the crystal-structure of the pristine ZnO nanopillars as well as those implanted with Au, Ag-ions. Rigaku SMARTLAB 9 kW instrument with rotating-anode generator and CuKα_1 characteristic radiation was used in our experiment and the diffractometer was equipped with a primary parabolic multi-layered mirror. In the middle-resolution (MR) set-up we used a linear detector on the secondary side; this setup was used for almost symmetric long-range $2\Theta/\omega$-scans. In these scans we avoided intense diffraction peaks of the Si substrate by introducing the angular offset of $\Theta - \omega = 5°$. The advantage of the MR setup consists in its high primary-beam intensity; however, a relatively large divergence of the primary beam makes it almost impossible to measure the size of coherent domains (mosaic blocks). For this purpose, we used a high-resolution (HR) setup, in which the primary x-ray mirror was combined with a channel-cut 2x220Ge monochromator. In this setup we measured reciprocal-space maps around the symmetrical reciprocal-lattice point 0002.

Rutherford Back-Scattering spectrometry (RBS) was used for elemental depth profiling in ZnO nanopillars using a beam of 2.0 MeV and 5.0 MeV He^+ ions from a Tandetron accelerator using the detector placed at a scattering angle of 170°. Two distinct He-ion energies were used in RBS to have higher depth resolution for elemental depth profiling in the ZnO layer (He-ion beam 2MeV) and complementarily to separate Ag, Au peaks in RBS spectrum (He-ion beam 5MeV). Simultaneously, all recorded sets of the RBS spectra for both energies were evaluated.

Scanning electron microscopy (SEM) with a field emission gun (SU5000 FE-SEM, Hitachi High-Tech Europe GmbH, Germany) and partially with a TESCAN MAIA 3 instrument with a field emission gun (TESCAN, Czech Republic) was used to observe surface morphology of the nanopillars. All samples were mounted on specimen stubs by double-sided adhesive carbon tape, placed into an electron microscope holder, and observed using a secondary electron detector under high vacuum at an accelerating voltage of 10 kV and 5 kV.

2.3. Optical analyses of ZnO nanopillars implanted with Au/Ag by spectroscopic ellipsometry (SE), photoluminescence (PL) and diffuse-reflectance spectroscopy (DRS)

The optical emission and absorption properties of ZnO nanopillars were addressed by combining three different spectroscopy methods collectively providing information on crystalline quality of nanopillars, validation of presence and optical activity of embedded metal NPs. Optical emission was characterized by photoluminescence (PL) spectroscopy measurements carried out at 10 K by employing a closed-cycle He refrigerator system and using a 325 nm wavelength He–Cd laser as an excitation source (power density ~20 W cm^2). The PL spectra were recorded by fiber-optic spectrometers (Ocean Optics HR4000/USB4000) with a spectral resolution below 2 nm. Optical absorption and scattering were inspected at room temperature by means of diffuse-reflectance spectroscopy (DRS) using EVO-600 (Thermo Fisher Scientific, Inc.) UV–Vis spectrophotometer. Note that DRS deals with absorption and scattering, the sum of which by definition is extinction; the latter is also one of the prime parameters in Spectroscopic Ellipsometry (SE), thus making DRS and SE measurements to a certain degree complimentary.

VASE ellipsometer (J.A. Woollam Co.) in the VIS-NIR spectral range for incidence angles of 40°–80° was used to collect the spectra of the ellipsometric parameters. Simultaneous reflectance measurements were performed using the same instrument and treated with the help of the commercial WVASE software. Spectroscopic ellipsometry, as an indirect characterization technique, requires a sample model and optical constants of the material in the form of table data or parameterized dielectric functions, see details in [30]. The ZnO nanopillar layer was modelled as a layer with a gradient profile of refractive index. Variation of voids across the nanopillar structure was accounted for by an effective medium (Maxwell-Garnett) approximation. The bottom part of the nanopillars was supposed to be formed by a compact ZnO film, whereas the top of the layer, due to the conical shape of nanopillars and their orientation, was expected to contain a negligible volume fraction of ZnO. Only limited spectral range (photon energy 0.7-3.0 eV) was selected for ellipsometry examination, first to ensure that the reflected beam dominantly contains specular contribution with low depolarization and second to simplify parameterization of ZnO electric permittivity. ZnO optical constants were parameterized by Cauchy dispersion relation extended with the ZnO exponential absorption edge [38]. The influence of ZnO nanopillar irradiation by the Au and Ag ions on their optical properties was modelled by an

additional Lorentz harmonic oscillators accounting for possible local surface plasmon resonances (SPR) [30, 38]. According to the SRIM calculations, amplitudes of these oscillators (that relates to the concentration of Au+Ag ions/nanoparticles) were supposed to vary across the layer. The Gaussian function was designed to approximate the real profile.

2.4. Photocatalytic properties

The photocatalytic properties of the pristine and implanted ZnO nanopillars were tested by degradation of an organic dye (Rhodamine B) in a water solution with the concentration 5 mg/l, under the UV-radiation by a measurement of optical absorption spectra. The ZnO nanopillars were submerged in Rhodamine B solution, placed under a 40 W UV-lamp (wavelength 254 nm) and irradiated up to 300 min. Additionally, we irradiated a reference solution containing only Rhodamine B without ZnO sample to see its own degradation under the UV light. The absorption optical spectra of Rhodamine B solution were measured in time with a step of 30 min during UV exposure by the UVISEL ellipsometer (75 W Xe lamp, Horiba, France) in the wavelength range of 450 – 650 nm with a step of 1 nm. The size of ellipsometer beam spot was 1200 μm.

3. Results

3.1. Theoretical SRIM simulations of Au-ion interaction with ZnO

SRIM calculations [39] of the Au-ion 400 keV and Ag-ion 252 keV depth profiles and the energy stopping in ZnO nanopillars have been provided. It must be taken into account that SRIM calculation is not capable to cover any morphological aspects of the sample such as crystallinity, surface roughness, porosity etc. which aspects would limit the simulation validity. Thus, a 500 nm thick ZnO bulk layer is taken into account in the calculation in **Fig. 1a**. We provided SRIM calculations of ion energy losses using an effective density of the ZnO nanopillar layer in **Fig. 1b**. The effective density of the ZnO nanopillar layer was estimated by using the ZnO layer thickness determined by RBS in atoms. cm^{-2} and by using the thickness determined from SEM cross-section measurement on pristine samples. The areal atomic density of the ZnO nanopillar layer of 2000 x 10^{15} atoms. cm^{-2}, taking into account Zn and O atoms, was measured by RBS for the pristine sample (see chapter 3.2, **Table 2**). SEM cross-section analysis gives us the thickness such as the vertical height of the ZnO nanopillar layer averaged over several SEM measurements being about 450 nm (taken as a perpendicular thickness of the nanopillar layer facing the penetrating ion implantation beam). Based on above described procedure, the effective average density of the ZnO nanopillar layer was evaluated being about 3.0 $g.cm^{-3}$ differing significantly from the density of bulk ZnO (5.61 $g.cm^{-3}$).

SRIM calculations of the Au-400 keV and Ag-252 keV ion energy stopping using bulk density and the effective ZnO layer density are presented for comparison in **Fig. 1a** and **Fig.1b,** respectively. SRIM prediction of Ag, Au-ions penetration depths using the effective ZnO nanopillar density is presented in **Fig. 1c**. Additionally, the Ag/Au projected ranges in ZnO nanopillars, with free spaces, would suffer a higher uncertainty due to the significant ion-energy straggling during the penetration through voids in the ZnO layer. However, we see that the penetration depth through the ZnO nanopillar layer is higher compared to bulk ZnO as well as the energy transfer less in the case of the lower density of the ZnO layer. This information are important for the correlation with optical parameter of the irradiated layer

such as extinction coefficient as it is presented later. We present also the SRIM calculation of vacancies created by Au and Ag ions implanted with energies of 400 and 252 keV, however it must be said that these numbers are valid independently for Au-ion implantation and Ag-ion implantation being calculated on fresh bulk ZnO with the effective density 3 g.cm^{-3}. We can see, that tens of vacancies per nm of depth are produced in ZnO per ion, where Au-ion produce about 3 times higher number of vacancies compared to Ag-ions as it was expected due to the distinct ion mass.

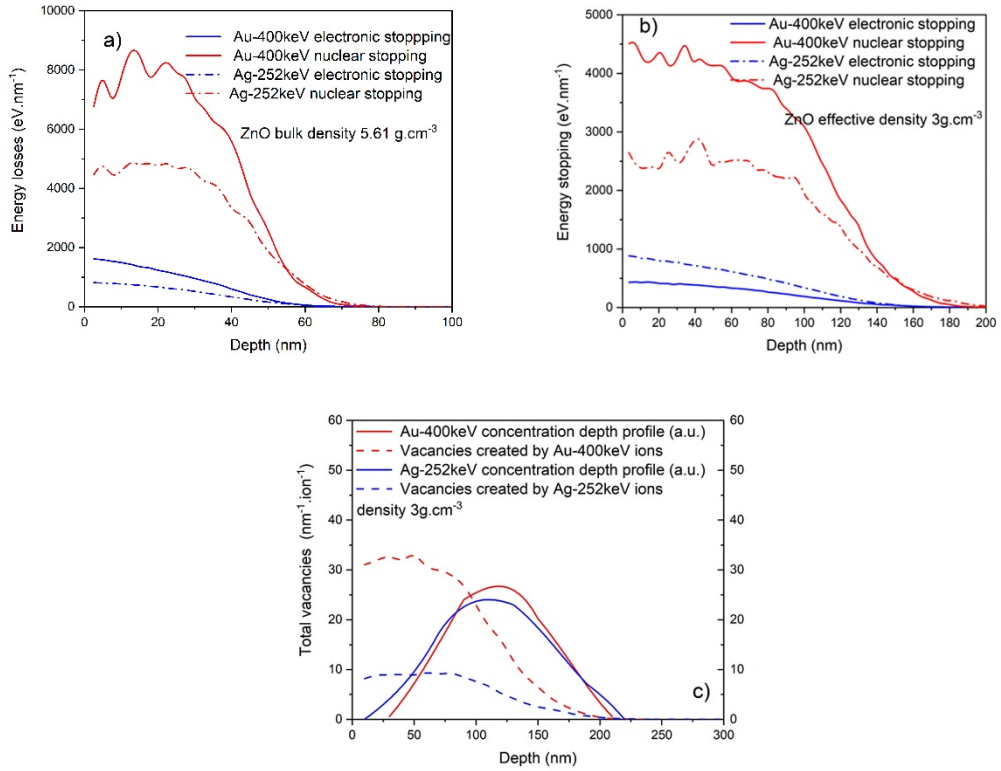

Figure 1

SRIM calculation of energy stopping of the Au-400keV and Ag-252keV ions with ZnO bulk density (5.61 g.cm^{-3}) and the effective density of the ZnO layer with nanopillars (3.0 g.cm^{-3}) in a) and b), respectively. SRIM calculation of Au, Ag concentration by Au-400keV and Ag-252keV ions in ZnO with the effective density of the ZnO nanopillar layer (3.0 g.cm^{-3}) in c). The total number of vacancies created in ZnO during ion implantation for Au and Ag ions is presented also in c).

3.2. Elemental and structure analysis by RBS and XRD

The recent results published in [23, 32, 40] can give us an idea of the distinct radiation damage accumulation, Au-NP coalescence and defect nature in various ZnO crystallographic orientations in bulk crystals. NP coalescence in ZnO nanopillars and their resulting optical response differ from ZnO bulk [30].

RBS analysis was used to follow, at least qualitatively, the Au and Ag concentration depth profiles in ZnO nanopillars. The RBS depth profiling of Ag/Au in ZnO nanopillars would be affected by complex morphology, high roughness, thus the depth scale calculation cannot be performed with the bulk ZnO density, but the effective density must be used. On the other hand, RBS offers qualitative information of the ZnO nanopillar layer thickness deposited on Si, where we see the modification of the Zn and O signal. Due to the content of two noble metals Ag and Au, two He-ion beam energies were used in RBS analysis, as it is justified in chapter 2.2. We compiled RBS data from both He-ion energies used for

measurement to make comprehensive characterization of Au, Ag integral amounts, depth profiles and ZnO layer thicknesses. Detailed part of elemental RBS spectra measured with He-5MeV of Zn, Ag and Au signals is presented in **Fig. 2a** normalized to the same cumulated charge. Au and Ag-depth profiles were determined and the results are presented in **Fig. 2b.** There, we observed a shift of the Au concentration maximum towards the ZnO surface with the increased Au-ion fluence, since Ag-amount remained constant.

In general, the metal depth profiles in the ZnO nanopillar layer measured by RBS are broader and exhibit an asymmetric distribution compared to the SRIM prediction. It was confirmed that the Au and Ag are distributed in ZnO nanopillars and coalescence can take a place within a major part of the nanopillars. RBS analysis is sensitive to surface morphology, where a complex morphology of the ZnO nanopillar layer can modify the elemental depth profiles by the typical in-depth tales at Au, Ag-depth profiles [41, 42]. We didn't present Au-depth profiles for the ZnO nanopillars solely implanted with Au-ions due to similarity of the presented Au-depth profiles in the Ag+Au implanted samples in **Fig. 2b**.

From RBS analysis, we estimated ZnO thicknesses in atoms.cm^{-2} including the total number of Zn and O atoms in the layer and the integral contents of Au and Ag; the results are summarized in **Table 2**. The integral contents of Au and Ag implanted in ZnO nanopillars are in a good agreement with the nominally implanted values. The ZnO nanopillar layer thickness decreases with the increased Au-ion fluence for the samples implanted solely with Au as it was observed also in [30] and a comparable decreasing trend is observed for the dually implanted ZnO nanopillars, although the total sum of the Au and Ag-ion fluences is higher. This depletion of atoms, under the Au, Ag-ion bombardment, manifests itself as degradation of the ZnO nanopillar layer as can be seen in the narrowing of the Zn peak in the RBS spectrum in **Fig. 2a**.

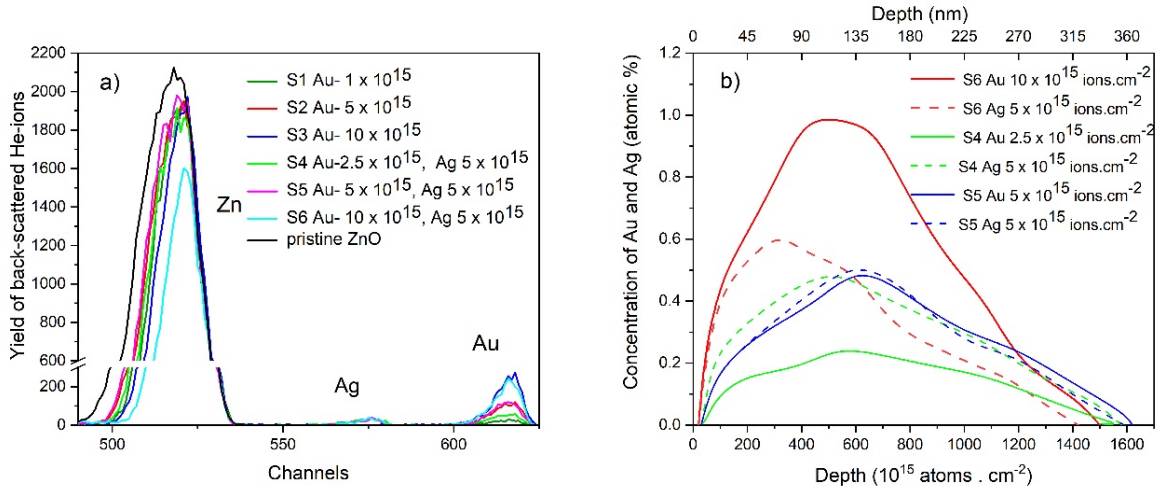

Figure 2

RBS-5MeV spectra of the pristine, and the as-implanted ZnO nanopillars implanted with Au-400 keV and Ag-252keV ions using various fluences - the normalized part of the RBS spectra with Zn, Ag and Au peaks in detail in a) and Au/Ag concentration depth profiles in ZnO nanopillars determined from RBS spectra b) with the depth scale in atoms.cm^{-2} and in nm using the effective ZnO nanopillar layer density 3g.cm^{-3} .

Sample/ion fluence (10^{15} atoms.cm^{-2})	Au integral amount (10^{15} atoms.cm^{-2})	Ag integral amount (10^{15} atoms.cm^{-2})	ZnO layer thickness (10^{15} atoms.cm^{-2})
S1/1 × 10^{15}	1.0 ± 0.2	-	1950 ± 200
S2/5 × 10^{15}	4.4 ± 0.2	-	1900 ± 200
S3/1 × 10^{16}	8.5 ± 0.2	-	1630 ± 200
P/Pristine	-	-	2000 ± 200
S4/ Ag-5 × 10^{15}+ Au-2.5 × 10^{15}	2.3 ± 0.2	4.4 ± 0.2	1980 ± 200
S5/ Ag-5 × 10^{15}+ Au-5 × 10^{15}	4.4 ± 0.2	4.3 ± 0.2	1980 ± 200
S6/ Ag-5 × 10^{15}+ Au-10 × 10^{15}	8.0 ± 0.2	4.4 ± 0.2	1420 ± 200

Table 2

RBS results showing the Au, Ag integral contents in ZnO nanopillars, ZnO layer thicknesses in atoms.cm^{-2} for the pristine and the implanted ZnO nanopillars at various ion implantation fluences.

XRD analysis of the ZnO nanopillars was carried out by using the MR $2\Theta/\omega$ scans. MR experiments offer much higher diffracted intensity giving opportunity to determine the ZnO lattice parameters from a large number of diffraction maxima with sufficient accuracy. Simultaneously, the MR measurements are suitable for searching possible Au-NP diffraction peaks. **Fig. 3** displays the $2\Theta/\omega$ scans after background subtraction, where all the ZnO diffraction maxima could be identified in the measured curves. In addition to the symmetric 00L ZnO peaks, other ZnO diffraction maxima can be found in the diffraction curves, which means that the ZnO layer does not exhibit any strong texture and most likely the nanopillars have random orientations. Au or Ag diffraction peaks were not resolved. The diffraction curves exhibit also a weak 0002 reflection in the position of the WKβ spectral line, present also in the primary beam, since no high-resolution monochromator was used. P, S1 – S6 denote the sample numbers as they are presented in **Table 2.** We observed enhanced increase of integrated intensities of diffraction maxima for S4-S6 samples, being much more promoted, compared to S1-S3 samples (see **Fig.3**). This effect would be connected to a slight difference between sample sets S1-S3 and S4-S6, but rather to deformation of ZnO nanopillars originally preferably oriented with the highest intensity for 0002 diffraction maxima in case of pristine sample and gradually enhancing of also other diffraction maxima. Thus we would suggest, that preferential nanopillar orientation is not so well defined in S4-S6 samples. Such an increase of lattice misorientation in S4-S6 compared to S1-S3 results in an increase of integrated intensity of diffraction.

We fitted the most intense ZnO diffraction maxima 0002, $10\bar{1}1$, $10\bar{1}2$, and $10\bar{1}3$ to Voigt functions and determined their exact positions. Using the well-known Cohen–Wagner approach modified for hexagonal crystals [43] from these positions we determined the ZnO *a* and *c* lattice parameters. The resulting values are summarized in **Fig 4**, along with their statistical errors.

The *c*-lattice parameter does not significantly change in the ZnO nanopillars after implantation within the estimated uncertainties. However, *a* lattice parameter slightly increases with the Au-ion fluence, where this enhancement depends mainly on the Au-ion fluence. Similar effect of compression in *c*-oriented facet of ZnO and contrary, expansion in *a*-plane facet have been observed in ZnO bulk irradiated samples as well in [23]. Implanted Au dopant preferably do not enter any substitutional position due to higher Au-ion radii [44], but rather is positioned in interstitial positions and create clusters. It is expectable that the ZnO will be modified preferably with heavier ions, however it is interesting, that dually Au, Ag-ion implanted samples exhibited the same or lesser structure modification even the sum of both ion fluences is equal or higher compared to the solely Au-ion

implanted samples (see **Fig. 4**). If some portion of this ions are Ag-ions with the lower mass, the radiation damage accumulation is not so pronounced. E.g. ZnO nanopillars implanted with Au-ions with the fluence 1×10^{16}cm^{-2} (S3) exhibited similar *c* lattice parameter as the sample implanted with Au, Ag-ions with the ion fluence in summary of 1.5×10^{16} cm^{-2} (S6). Similarly, the sample Au-ion implanted with 5×10^{15}cm^{-2} (S2) compared to Ag, Au-ion implanted with 7.5×10^{15}cm^{-2} (S4) – see **Table 2** and **Fig. 4.** In general, *a* lattice parameter exhibited larger variations, however it is slightly higher for S6 compared to S3 sample, but very closely in the frame of the uncertainty. This lattice parameter does not exhibit significant trend with the ion implantation fluence which might be connected to the complex defect accumulation accompanied by surface morphology modification which was studied also by SEM and partially it would be deduced from XRD long-range scans.

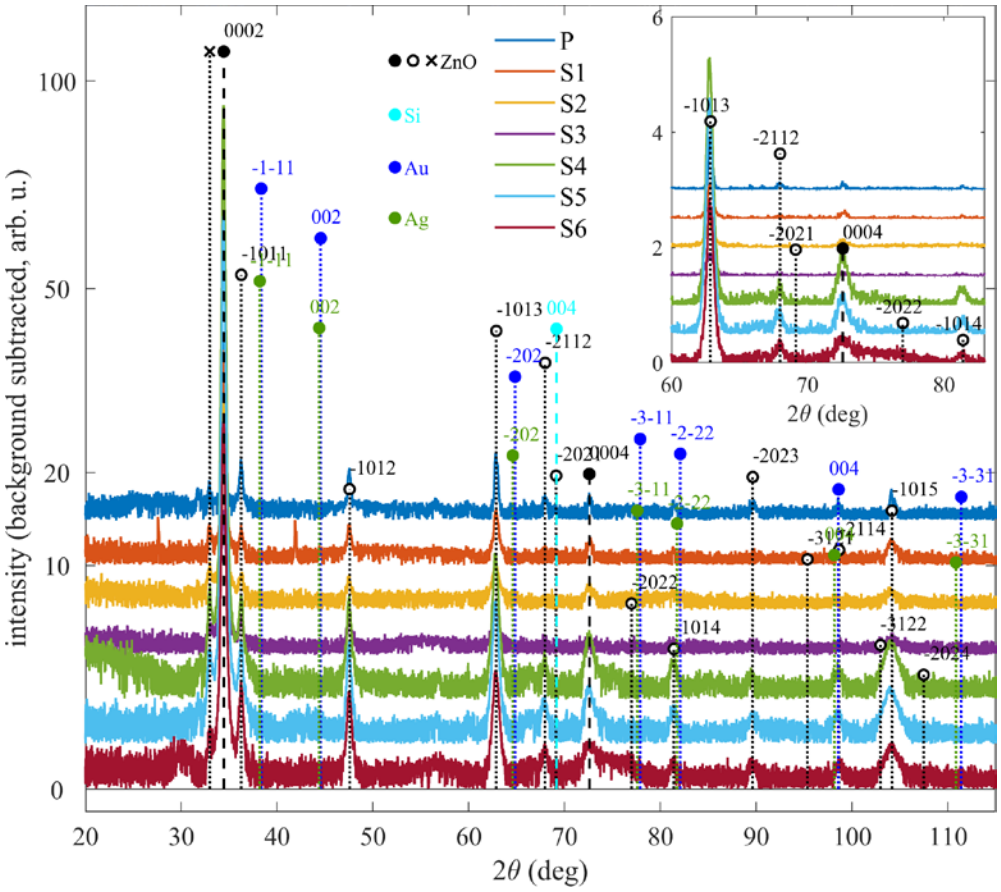

Figure 3

Medium-resolution 2Θ/ω long scans measured for pristine and the Au, Au+Ag-implanted are presented with the theoretical positions of diffraction maxima ZnO (black), Ag (green), Au (blue), and Si (cyan). The full black dots denote the 000L maxima of ZnO, while the open black circles represent all other ZnO diffraction maxima. The black cross denotes the position of the 002 reflex of ZnO for the WKβ spectral line, which is also present in the primary radiation. The inset displays the range of 2Θ between 60 and 83 deg in more detail. In both graphs, the curves are shifted vertically for clarity. In order to improve the visibility of weak peaks, in the main graph the vertical axis is proportional to square-root of intensity.

To follow this trend more in details, we determined the mean vertical sizes of the coherent domains in the ZnO nanopillars from the integral widths of diffraction maxima 0002 and 0004. In order to minimize the influence of limited angular resolution in the MR setup, we measured reciprocal-space maps around these diffraction maxima in the HR setup and determined the integral widths of the reflexes by numerical integration along the ω axis. We used the approach presented in [30], where we assumed that the domains are uniaxial ellipsoids oriented along the [0001] and we reformulated the Williamson–Hall approach [43] for ellipsoidal domains. The vertical domain radii *L* as a function of Au, Ag-ion implantation fluence is presented in **Fig. 5**. We can follow the decreasing trend of the vertical mean size of vertical domains with the increasing total Ag+Au-ion fluence exhibiting sort of saturation above 7.5 × 10^{15}cm^{-2}, the vertical domain radii are kept below 50 nm.

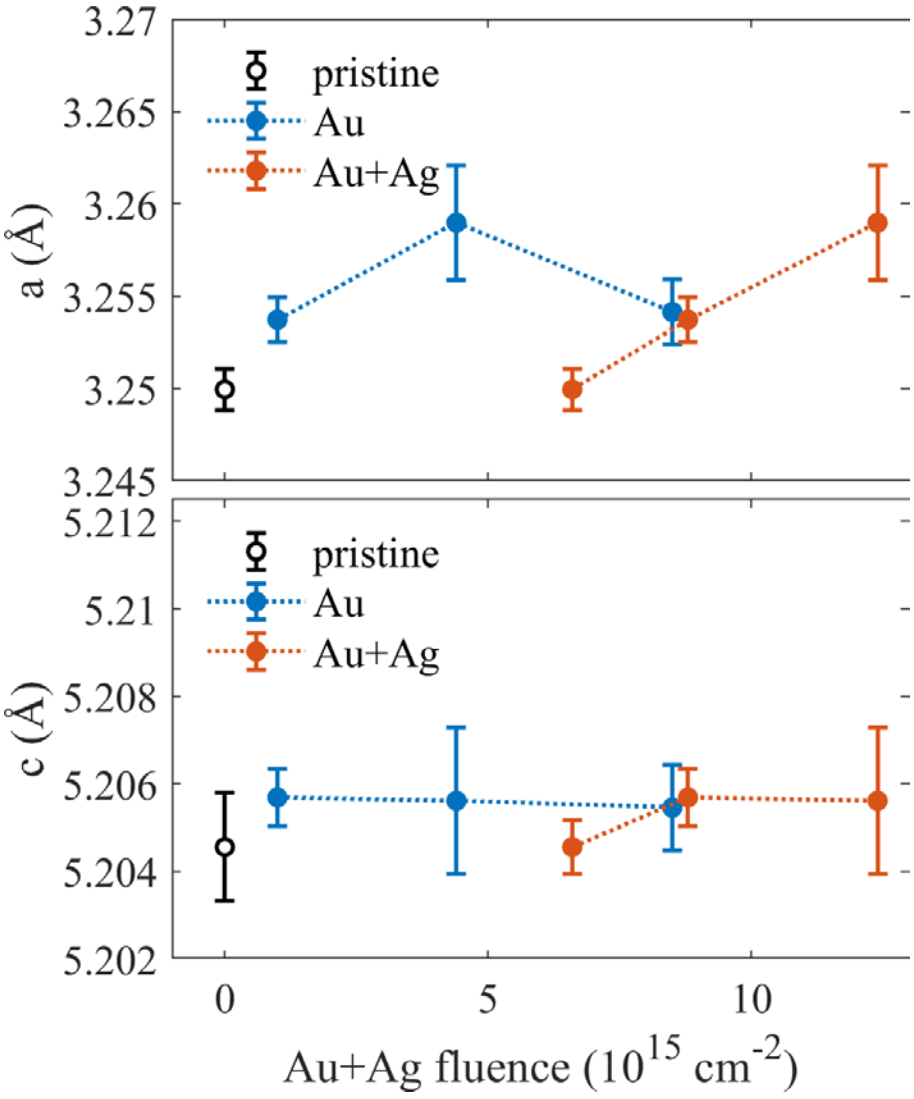

Figure 4

Lattice parameters a and c of the ZnO nanopilars determined from the position of the ZnO reflexes 0002, $10\bar{1}1$, $10\bar{1}2$, *and* $10\bar{1}3$ *as a function of the total Ag+Au-ion implantation fluence. Blue curve shows the Au-ion implanted samples (S1, S2, S3) and orange curve shows the Ag+Au-ion implanted samples (S4, S5, S6), respectively.*

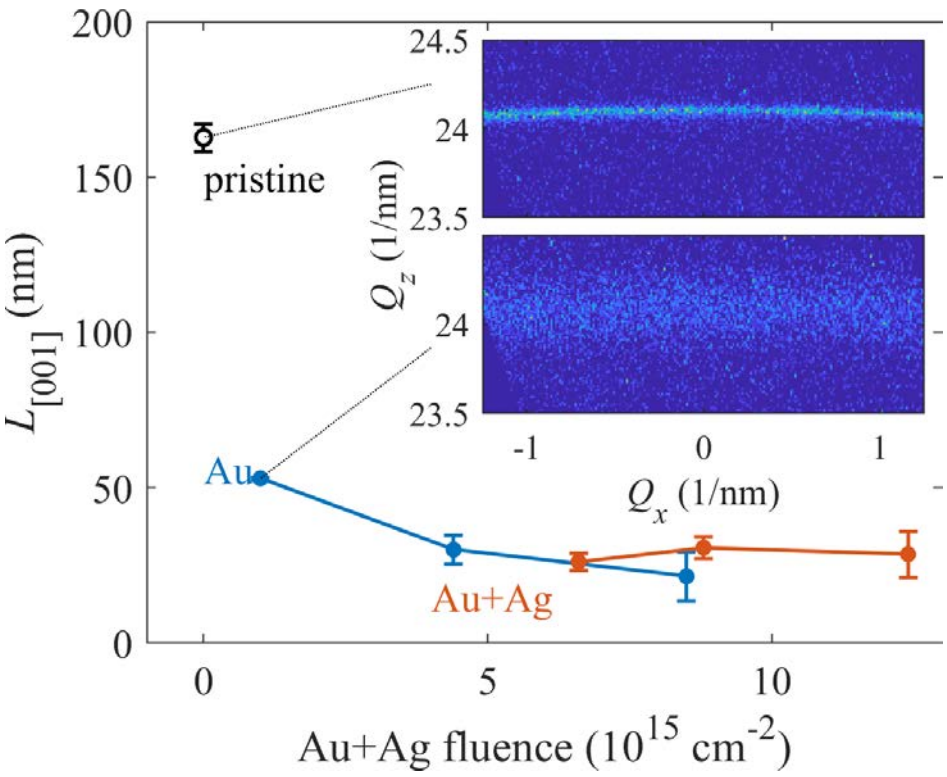

Figure 5

Vertical domain radii L determined from the HR reciprocal space maps around the diffraction maxima 0002 and 0004 as a function of the Au-ion implantation fluence for the Au-implanted ZnO nanorods (blue curve) and for Au+ Ag-implanted (red curve). Blue curve shows the Au-ion implanted samples (S1, S2, S3) and orange curve shows the Ag+Au-ion implanted samples (S4,S5, S6), respectively. The x-axis is the total ion implantation fluence. P stands for the pristine sample. The insets show the examples of the 0002 reciprocal-space maps of the pristine sample (upper panel) and sample S1 (lower panel).

3.3. ZnO nanopillars morphology (SEM analysis)

Surface morphology was investigated by SEM. The SEM images of the ZnO nanopillars grown on silicon substrates and their morphology are presented in **Fig. 6.** SEM visualized morphologies of the pristine sample and the samples after the Au-400 keV, Ag-252 keV ion implantation are presented with the ascending Au-ion fluence in **Fig. 5 b, c** and **d**, respectively. Uniformly distributed nanopillars with the upper defined hexagonal facets are observed being grown vertically on the Si substrates, but some bending of the perpendicularly oriented nanopillars appeared in the pristine sample (see **Fig. 6a**). Morphology deterioration caused by accumulation of radiation defects proceeds to larger extent in the ZnO nanopillars implanted solely with Au-ions compared to combined implantation with Ag, Au ions compare **Fig. 6c** and **6d** for Au-ion fluence 5 × 10^{15}cm^{-2} and **Fig. 6d** and **6f** for Au-ion fluence 1 × 10^{16} cm^{-2}. The morphology degradation is exhibited by less-distinguished separated nanopillars which undergo such kind of interconnecting and melting being significant mainly for the highest cumulated

implantation fluence (compare e.g**. Figs. 6a** and **6d**). However, the ZnO nanopillar morphology is to a higher extent preserved for low and medium Au, Ag ion fluences.

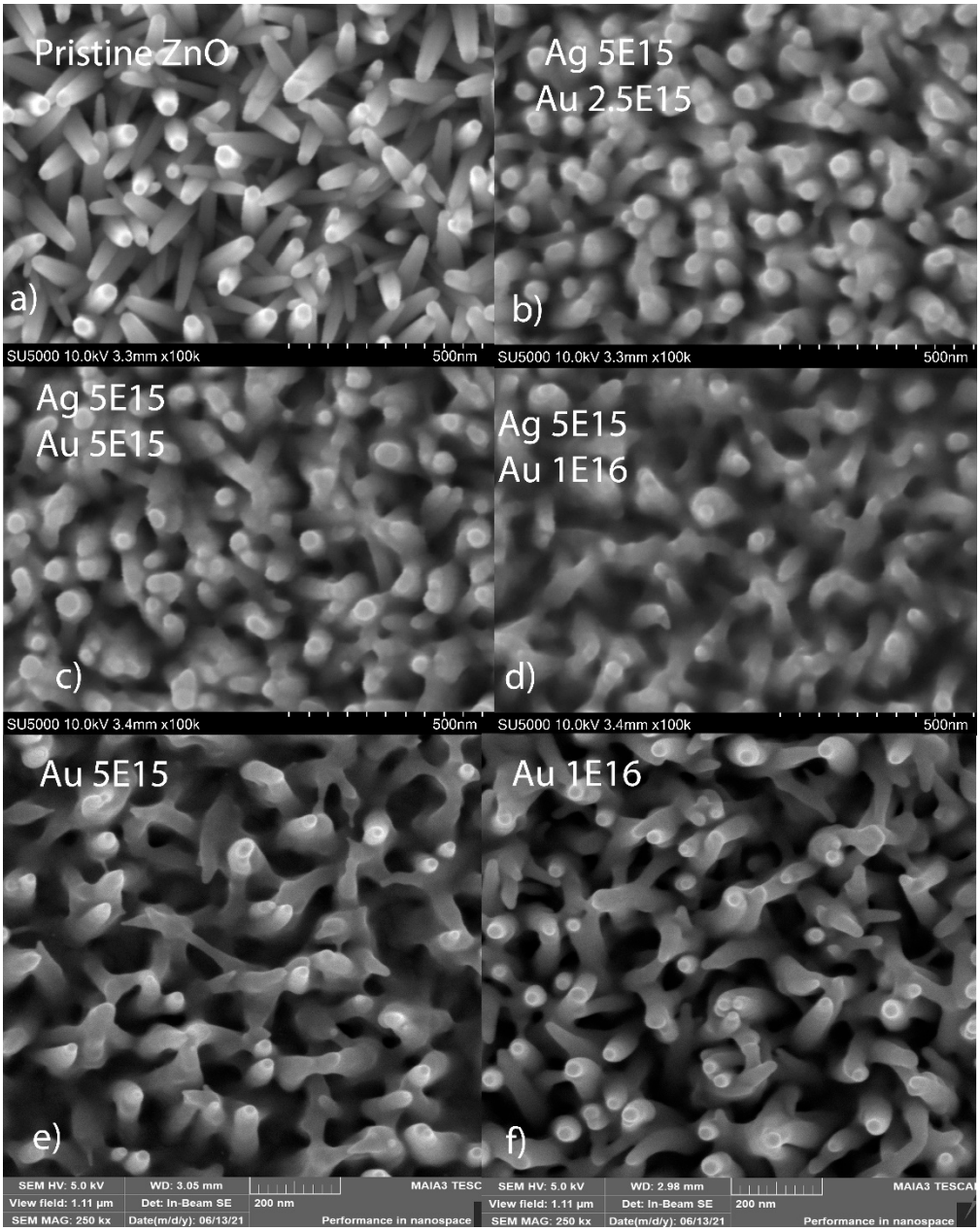

Figure 6

SEM analysis of the surface of the pristine ZnO nanopillars and as-implanted with the Au-400keV ions with fluences of 2.5 × 10^{15}, 5 × 10^{15}, 1 × 10^{16} cm^{-2} and Ag-252keV 5 × 10^{15} cm^{-2} in a), b), c) and d), respectively. ZnO nanopillars solely implanted with Au-ion with ion fluences 5 × 10^{15} and 1 × 10^{16} cm^{-2} in e) and f), respectively.

3.4. Optical properties of Au, Ag doped ZnO nanopillars

Optical emission and absorption properties of the ZnO nanopillars co-implanted with Au-400keV and Ag-252keV ions were analyzed by photoluminescence (PL) and diffuse-reflectance spectroscopy (DRS) techniques. In the present study, we focus on the optical properties of co-implanted ZnO nanopillars taking into account our recently reported observations of optical activity in solely Au-implanted ZnO nanopillars [30]. **Figure 7** summarizes the results of the PL measurements carried out at 10K on ZnO nanopillars co-implanted with Ag and Au ions with a variable Au implantation fluence. Note that Ag implantation fluence is constant $5 \times 10^{15} cm^{-2}$ for all the samples. First, we should point out the salient feature of PL emission, which is found spatially-inhomogeneous as illustrated by the PL pattern on the Inset in **Fig.7a**, where an array of relatively widely-separated bright-spots can be observed against a darker background.

The PL spectra collected from the bright-spots and the background areas (off the bright-spots) for different Au implantation fluence are presented in **Fig.7a** and **Fig.7b**, respectively. As one can see, the bright-spots exhibit spectral features that markedly differ from the background emission and thus cannot be considered as merely light-scattering centers. Also dissimilar is the variation of PL yield (quantum efficiency) with the increase of Au fluence from the background areas decreasing steadily while the bright-spot emission is reaching a peak at intermediate (5×10^{15} cm^{-2}) fluence (cf. **Fig.7a** and **Fig.7b**). The broad PL spectrum of a bright-spot apparently comprises several partially overlapping components, also sharing some common features with the background emission and with pristine ZnO nanopillars. In order to expose the solely Au-implantation induced spectral changes, the differential PL spectra are built by dividing the bright-spot spectra at different fluences by that of the pristine (non-implanted) ZnO nanopillars and presented in **Fig. 7c**.

The pristine ZnO nanopillars exhibit features in PL spectrum typical to high-crystallinity ZnO with an intense narrow near-band-edge (NBE) peak at 368 nm (3.37 eV) related to exciton recombination dominating over a broad deep level emission (DLE) centered at around 600 nm (2.1 eV) originating from luminescent deep defect sites. The red luminescence (RL) component prevailing in the DLE is usually associated with V_{Zn}, Zn_i and O_i point defects [27, 45]. For all Au-implantation fluencies, the NBE appears totally suppressed in both bright-spot and background PL spectra, whereas significant changes occur in the lower-energy region of blue luminescence (BL) at around 2.8eV and green luminescence (GL) at around 2.5eV, respectively. While absence of excitonic NBE peak is common for as-implanted ZnO, the fact that the suppressed NBE is accompanied by the enhanced GL and BL might signify an efficient energy transfer to plasmonic Au-Ag nanoparticles. The spectral regions of BL and GL enhancement fall well within the reported surface plasmon resonance (SPR) activity range of Ag and Au NPs (highlighted by shaded areas in **Fig.7**) [46, 47]. Indeed, SPR is a complex effect that modifies light coupling with a medium containing embedded metallic NPs. The excitation of SPR in such NPs results in an extreme concentration of light and an enhanced electric field around the nanostructures, leading to the significant enhancement in absorption and scattering efficiencies for photons at the resonant energy [48].

The light-scattering phenomenon was addressed independently by means the diffuse-reflectance spectroscopy (DRS), where the detected signal, being directly proportional to the scattering efficiency, has provided a measure of SPR effect for different implantation fluencies. The differential DRS spectra presented in **Fig. 8a** are built by dividing each diffuse-reflectance spectrum by that of the pristine (non-implanted) ZnO nanopillars, and in this way exposing only Au-implantation induced changes. The two spectral regions of the enhanced scattering at around 2.9eV and 2.1eV match well with those typically

ascribed to Ag and Au SPR activity as well as with the enhanced BL and GL emission in **Fig. 7**, thus supporting their possibly common plasmonic nature. It is noteworthy in this regard that solely Au-ion implanted ZnO nanorods exhibit single maximum in DRS as well as in PL spectra positioned at around 2.5 eV (500-550 nm) [30]. Taking all this into consideration, the two distinctive SPR maxima in **Fig. 8a** point toward coexistence of Au and Ag nanoparticles for Au-ion fluences up to $5\times10^{15}cm^{-2}$. A more detailed insight into the origins of this effect is provided by SE analysis and discussed in the subsequent section.

As a final point, we note that in absence of the excitonic NBE features in the PL spectra, DRS has provided an alternative way for assessing the optical bandgap variation as a function of Au-implantation fluence from the absorption edge position in the Tauc plot presented in **Fig.8b**. Considering the absorption edge (bandgap) of a bulk ZnO crystal (3.28eV) as a reference, the pristine ZnO nanorods demonstrate notably blue-shifted (3.32eV) values, which increase further for the Au-implanted ZnO nanorods in correlation with the Au-implantation fluence and reaching up to 3.37eV.

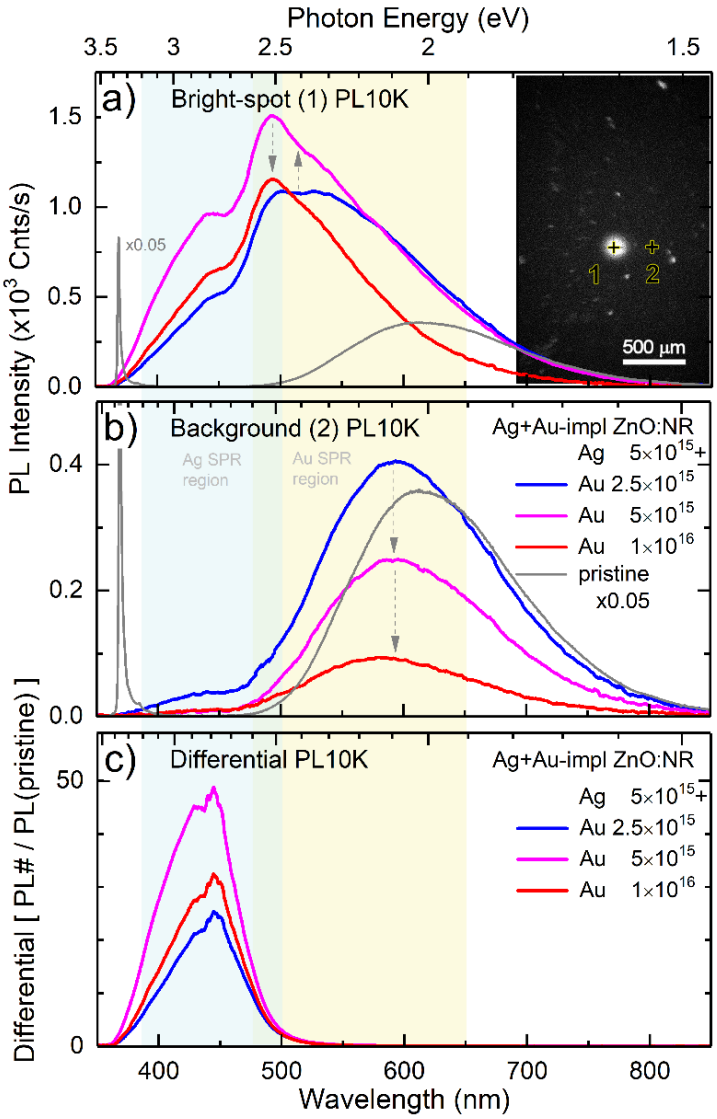

Figure 7

Low-temperature PL spectroscopy (10K) of the ZnO nanorods co-implanted with Ag-ions of $5\times10^{15}cm^{-2}$ and Au-ions of variable fluence in a). PL spectra collected from the bright-spots. Inset illustrates the inhomogeneity of emission pattern with the indicated PL probe positions (+ markers) corresponding to the bright-spot (1) and background (2) emission, respectively. The excitation laser beam (FWHM ~ 180µm) is superimposed with one of the bright-spots in b). PL spectra collected from the background area (off bright-spot) in c). Differential PL spectra of the bright-spots with varying Au-implantation fluence. Shaded color-coded areas highlight spectral regions typically ascribed to Ag and Au SPR activity.

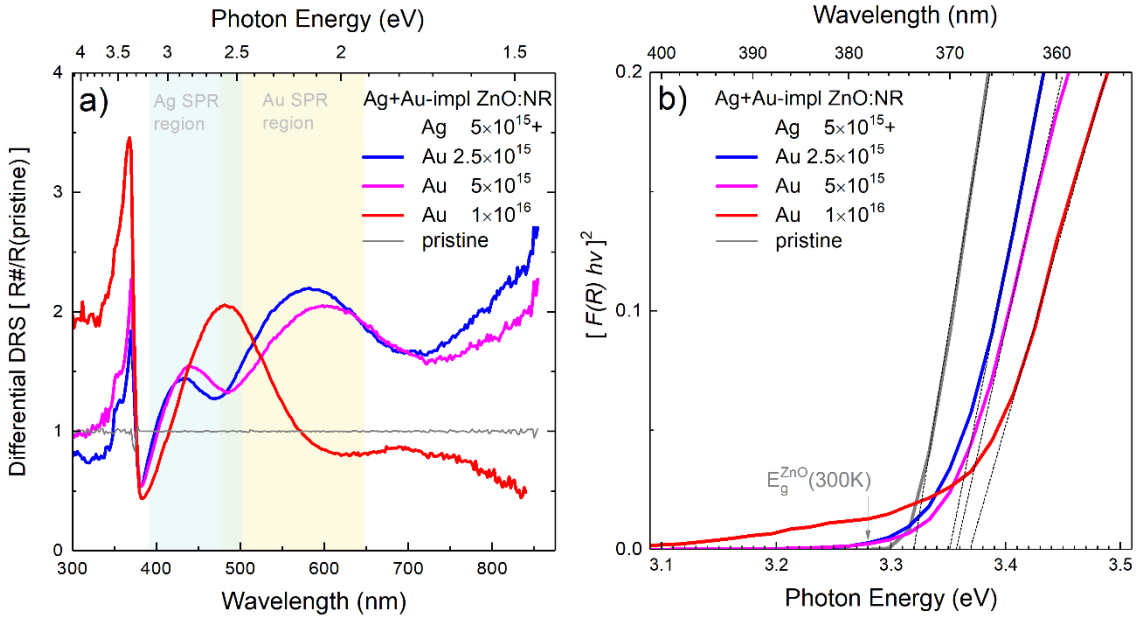

Figure 8

Diffuse-reflectance spectroscopy (300K) of the ZnO nanorods co-implanted with Ag-ions of $5\times10^{15}cm^{-2}$ and Au-ions of variable fluence. a) Differential DRS spectra built with reference to pristine (non-implanted) ZnO nanopillars. b) Tauc plot for direct optical transitions revealing variation of the optical absorption edge with Au implantation fluence.

Spectroscopic ellipsometry was employed to follow the structural modification in ZnO nanopillars as well as the optical parameters (refractive index and extinction coefficients). It was found that the refractive index in the pristine, as well as in the Au, Ag-ion implanted ZnO nanopillars (**Fig. 9a-d**), exhibited a gradual decrease from ZnO bulk value (close to the substrate) toward ambient-like value on the surface. This is a result of the graded transition introduced by the specific layer morphology: shape, density and orientation of nanopillars. Additionally, the implanted ZnO nanopillars showed the depth profiles of the refractive index, where we observed the decrease of the refractive index in the upper part of the ZnO nanopillars (150–300 nm in the retrograde scale see **Fig. 9**) with the increased Ag and Au-ion fluence. The SRIM calculated projected range of the Au-400keV and Ag-252keV ions is about 100 nm below the ZnO layer surface which means about 300 nm in the retrograde depth scale used in **Fig. 9**. The RBS measurement identified the Au, Ag depth distributions even broader than predicted (see **Fig. 2c**).

Spectra of the extinction coefficient of Au/Au+Ag ions irradiated ZnO nanopillars typically featured one (Au ions) or two (Au+Ag ions) oscillators that were not detected for the pristine sample. The corresponding oscillator energies have been observed at 1.8-1.9 eV (wavelength of about 670nm) in the case of Au ions irradiation (see **Fig. 9** – left panel, S1-S3 samples) and also at 2.8-2.9 eV (wavelength of about 430nm) for the combined Au and Ag-ion irradiation (see **Fig. 9** – right panel, S4-S6 samples). The depth profiles of the extinction coefficient across the film for identified resonant frequencies are plotted in **Fig. 9**. We observed also, that the absorption followed for the wavelength of 440 nm (2.8 eV) seemed to be positioned into the higher depth within the ZnO nanorod layer with the increased Au-ion fluence (see **Fig. 9** – S4-S6 samples) and simultaneously the ZnO layer thickness decreases which is obvious for the highest Au-ion fluence in **Fig. 9** – S1-S3 samples. The two absorption maxima are evidenced in the Ag+Au ion implanted samples (see **Fig. 9** - S4-S5 samples) in the same depth of the ZnO nanopillar layer with the pronounced shift to the deeper position for the enhanced Ag+Au-ion fluence. It would be concluded, that SE results confirmed PL analysis, showing distinct response in Au-ion implanted samples exhibiting maximum around 1.8 – 1.9 eV only, contrary Ag+Au-ion implanted samples showing two maxima around 1.8 – 1.9 eV and around 2.8 – 2.9 eV for the lowest and medium Au-ion fluence.

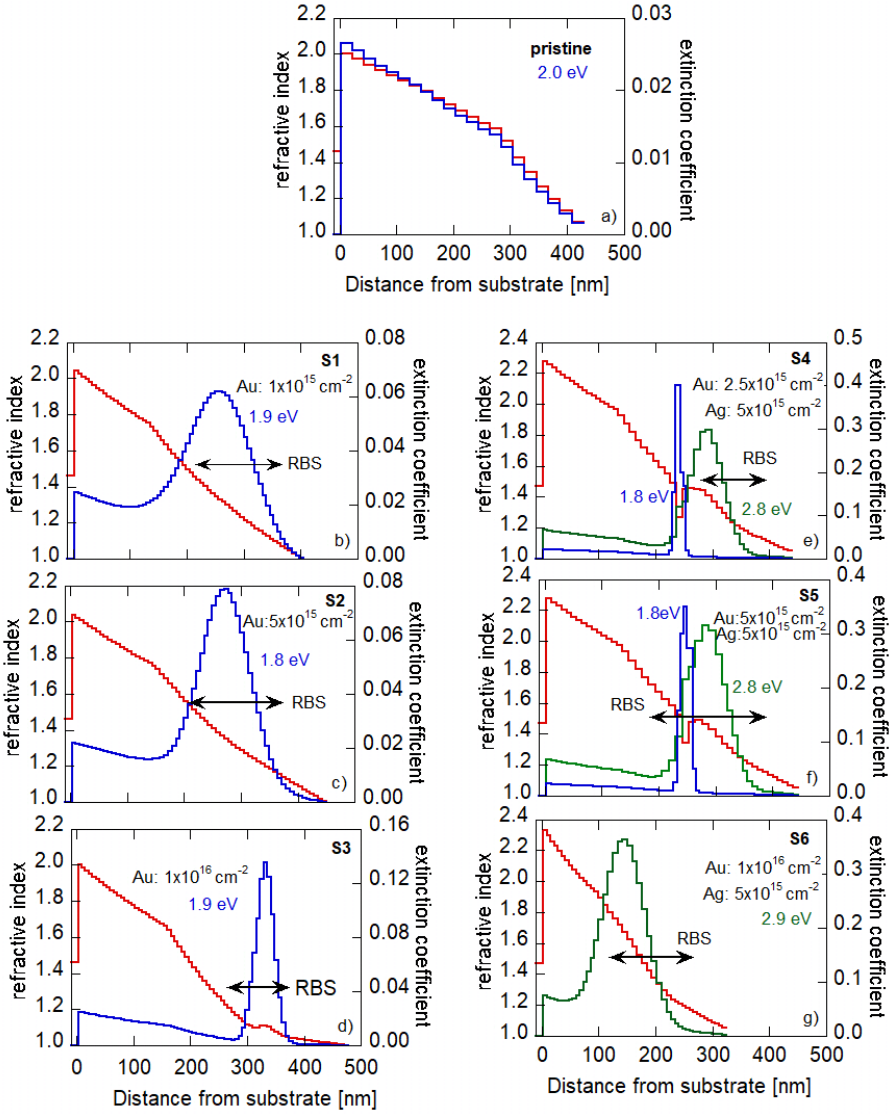

Figure 9

Depth profiles of the refractive index (red lines) and the extinction coefficient (blue and green lines) obtained by spectroscopic ellipsometry. The profiles are indicated for the photon energies where the SPR were identified (1.8, 1.9, and 2.8 eV). The black arrows roughly indicate the depth of Ag and/or Au-implanted layer as it was determined by RBS.

3.5. Photocatalytic activity

The photocatalytic activity was investigated via organic dye (Rhodamine B) degradation activity under the UV-light irradiation at 240 nm wavelength. It is important to say, that ion implantation enables twofold effect influencing photocatalytic properties. Firstly, extended optical absorbance in a broader wavelength range would be introduced via radiation defect, secondly possible noble metal aggregation and morphology modification (e.g. nanoroughnening effect) of nanorods. On the other hand, as these effects are synergic and complex, they can play beneficial as well as detrimental role. We observed, that the optical absorbance of the Rhodamine B solution evaluated by optical absorbance in the wavelength range of 400 – 600 nm, decreased faster in the case of the ZnO nanopillars present in the solution compared to the pure Rhodamine solution. The degradation was analyzed using the concentration ratio of the solution with the analyzed ZnO sample and the solution of pure Rhodamine B meant C/C_0 as a function of time. We can derive the degradation constant using a first-order kinetic equation $ln(C/C_0) = kt$, which corresponds to the photocatalytic degradation, where C_0 is the initial Rhodamine B concentration, C is the final concentration at time t and k is the apparent degradation rate constant. We present the degradation rate kinetics in the Au-implanted as well as Au, Ag-implanted samples. We used $ln(A/A_0)$, where optical absorbance A integrated in the wavelength range 400 – 600 nm has been normalized to A_0 , the nominal optical absorbance of the pure Rhodamine. The slope of the linear plot of $ln(C/C_0)$ or consequently $ln(A/A_0)$ versus time gives the apparent rate constant k. The plot of $ln(A/A_0)$ as a function of UV-light irradiation time is presented in **Fig. 10**. A similar approach has already been used in [50].

The kinetics of photocatalysis of Rhodamine B by the Au-ion implanted ZnO nanopillars is presented in **Fig. 10a**, where we see the strongest degradation for the pristine ZnO nanorods compared to the implanted samples with Au-ions (**Fig. 10a**) or Ag+Au-ions (**Fig. 10b**). The Au-ion implanted nanopillars exhibited less photocatalytic activity than the pristine ZnO nanopillars probably due to the radiation damage and consequent morphology deterioration. However, the degradation activity of the organic dyes is still more intense compared to the pure solution. Better comparison would be available via presentation of the degradation constant k for all samples, as it is presented in **Fig. 10c**. There are seen a decrease of photocatalytic activity for the both implanted ZnO nanopillar sets with the enhanced ion implantation fluence. Such effect seems to be slightly less pronounced for Ag+Au-ion implanted samples. However, the results are observed only for the wavelength specifically in UV region, where the absorption would not be optimal, thus additional testing in the wavelengths appropriate for the modified nanopillars will proceed.

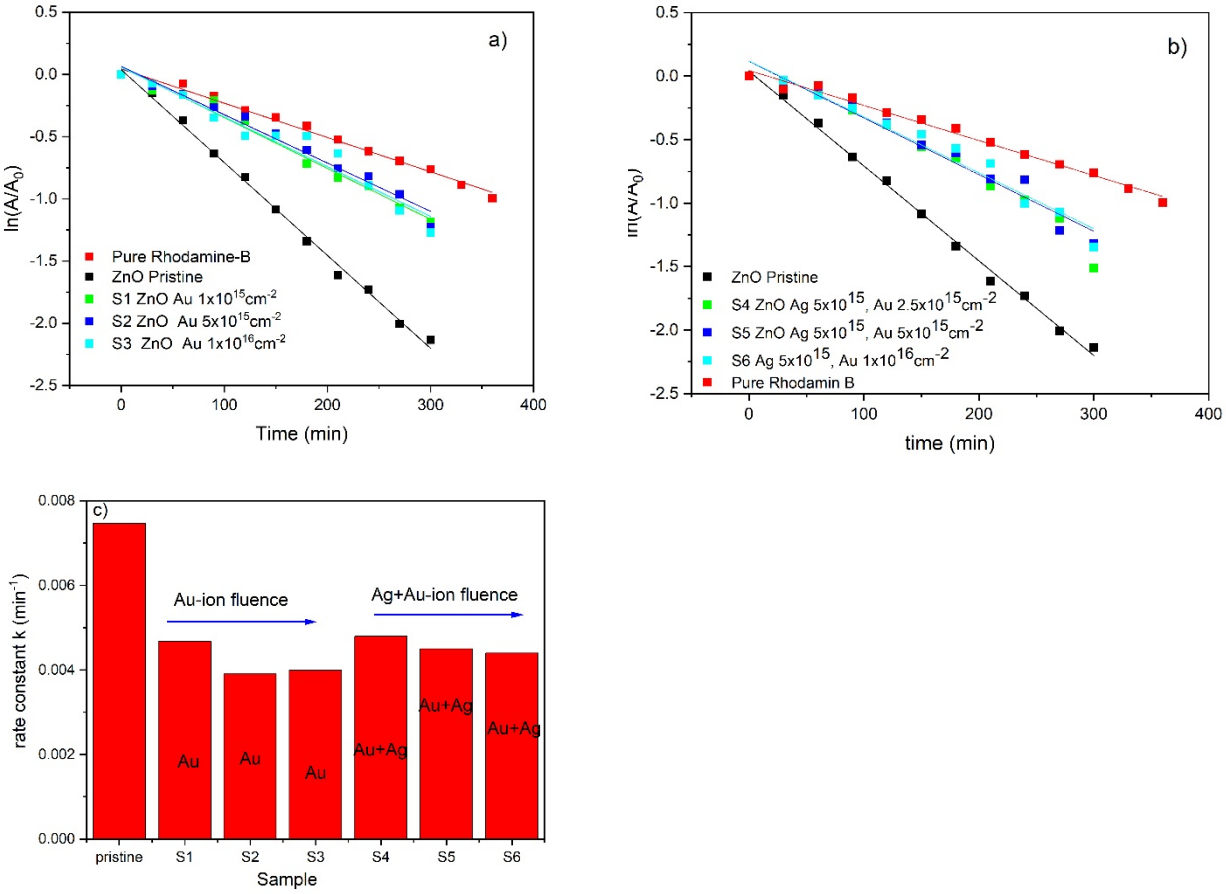

Figure 10 *Photocatalytic activity of ZnO nanopillars – the pristine sample and Ag, Au implanted samples. Photocatalytic kinetics is presented as the relative absorbance ln(A/A$_0$) in the chosen wavelength interval (400 – 600 nm) being function of time for pure Rhodamine solution, pristine ZnO nanopillars and ZnO nanopillars implanted by various Au-ion fluences in a) and Ag, Au-ion implanted nanopillars in b). Rate constant k is presented for all investigated samples in c).*

4. Discussion

We are presenting the study of ZnO nanopillars implanted with the Au-400 keV and Ag-252 keV ions. Ion implantation using medium ion-energies ensures, that Ag/Au will be embedded in the ZnO nanopillar layer, as it was predicted by SRIM. Thus we can expect direct incorporation of NPs in ZnO nanopillars interior which might be compared to other deposition possibilities using chemical attachment of NPs on the nanostructure surface [34]. On the other hand, in case of heavier ions with medium energies, we can expect dominating nuclear stopping with ballistic processes along the whole ion path. Nuclear collisions will create point defects mainly vacancies and interstitials. Simultaneously, ion implantation will degrade the crystallinity of the ZnO. The energy of penetrating ions during ion implantation will be released also in the form of heat and phonons.

Contrary, ZnO nanostructures are so promising due to a very high effective surface compared to ZnO bulk, which can serve as an effective sink for radiation defects, thus defect annihilation would be more effective in nanostructures compared to bulk [25-27]. Optical properties are strongly connected to the radiation damage accumulation which in consequence influence, via nanopillar morphology

deterioration, the photocatalytic properties and the effective surface area as well. However, these two effects might have interesting synergies, especially in connection to the noble metal nanoparticle created inside the ZnO nanopillars [37, 47, 51].

RBS identified Au, Ag species embedded in the ZnO nanopillar layer more broadly distributed than it was predicted. Ion implantation into the porous layer causes the uncertainty of noble metal depth incorporation as well as consequent depth profiling in the layer with significant roughness and porosity is very complex. However, RBS qualitatively showed that Au, Ag species are incorporated in the depth in reasonable agreement with SE analysis, showing the decreasing refractive index in the depth appropriately containing implanted ions. RBS and SE also confirmed a ZnO nanopillar layer decrease in thickness with increased Au-ion fluence. This trend has been observed similarly for the nanopillars implanted solely with Au-ions as well as co-implanted with Au, Ag ions. Interestingly, even if the total implantation fluence was higher in co-implanted samples, as the portion of ions was realized with much lighter Ag-ions, the final ZnO layer depletion was comparable to Au-ion implanted nanopillars.

These findings were supported with RBS analysis, where we observed a decrease in ZnO layer thickness, and SEM confirmed modification of the ZnO nanopillar morphology with increasing Au ion fluence, evidenced by a kind of erosion of the upper ZnO nanopillar and melting of the nanopillar bases. Such effect has already been observed for Au-implanted nanopillars with lower ion fluences [30] compared to co-implanted ion fluences at Au, Ag-implanted samples. Such nanopillar degradation and nanopillar side-wall modification have been observed in the N-ion irradiated ZnO nanorods in a broad ion fluence range in [29]. Also, XRD analysis supported this trend, where nanopillars having polycrystalline character exhibited with increasing Au-ion fluence a significant decrease of vertical domain sizes in response to radiation defect accumulation. Point defects accumulated at the domain borders compressed and decreased the domain sizes. The dislocation density is suggested to increase with decreasing domain sizes evidenced by XRD after implantation. Introduced strain can be connected to the evidenced band gap blue shift measured by DRS in the Ag, Au-implanted nanopillars. NBE blue shift to the lower wavelengths has been observed with the increasing Au-ion fluence in the ZnO nanopillars treated by Au-ions [30] and by He-ion bombardment as a consequence of the introduced radiation induced strain in [51].

For all Au-implantation fluences, the NBE appears suppressed in both bright-spot and background PL spectra, whereas significant enhancement occurs in the lower-energy region of blue luminescence (BL) at around 2.8eV and green luminescence (GL) at around 2.5eV, respectively. BL has been ascribed to radiation defects on ZnO nanorod surfaces irradiated with hydrogen in [49], because this BL disappeared after the annealing and/or after the surface passivation. On the other hand, the annealing at 750°C for 15 min after the Au-ion implantation of ZnO nanopillars didn't reduce BL, just contrary, with simultaneous strong absorption band occurrence in SE spectrum around 500 – 600 nm in [30], where it would be ascribed to Au-coalescence. It is suggested interplay of radiation defects and Au-coalescence, but arguments for Au-coalescence would be found in the differences of differential PL spectra between bright spots and dark areas (Au-NPs and ZnO with radiation defects, respectively).

SPR activity of the Au nanoparticles in the ZnO nanopillars was proved by SE, where the distinct extinction maxima (SPR) for Au-solely implanted and Ag+Au dually implanted were observed being located in the region with the decreased refractive index. Thus in the ZnO nanopillar layer depth, where the main localization of Ag, Au dopant is expected in connection to SRIM simulations and RBS analysis. SE identified interesting trend dually in the Ag, Au-implanted ZnO nanopillars, where for the lower Au-ion fluences two maxima appeared at wavelengths of about 440 and 680 nm (2.9eV and 1.8eV),

respectively. At the highest Au-ion fluence and Ag-fluence remained constant, SPR maximum at the energy of 2.8eV in between these two wavelengths appeared. Simultaneously, DRS analysis shows similarly that the two spectral regions of the enhanced scattering (at around 2.9 eV and 2.1 eV) match well with those typically ascribed to Ag and Au SPR activity as well as with the enhanced BL and GL emission, thus supporting their possibly common plasmonic nature.

Ag-nanoparticles exhibited optical absorbance in the wavelength range of 400 -550 nm depending on Ag-nanoparticle complexity [52]. Au nanoparticle shape, size, complexity and agglomeration influenced the absorption maximum being evidenced from 520–600 nm [53]. SPR in $Au_xAg_{(1-x)}$ alloy nanoparticles can be tuned with varying mole fraction of the particular metal which extend the SPR over a broad range of the UV–vis spectra with SPR red-shifting for the larger particle sizes. The $Au_xAg_{(1-x)}$ alloy nanoparticles with varying mole fractions show only one plasmon absorption peak and similar plasmonic strength as composite Au and Ag metals. The plasmon band shift changes linearly with increasing mole fractions of metal [52, 54]. In our case, DRS and SE evidenced two SPRs at the distinct wavelengths (according to the wavelength range of the Ag-SPR and Au-SPR) for the lower Au-ion fluences. Surprisingly, one SPR for the highest Au-ion fluence shifted to the wavelength in between these two SPRs appeared.

PL evidenced optical active bright spots on ZnO nanopillars exhibiting high optical activity in the wavelength region of 400 – 500 nm. It seems to be rather evidence of Ag-core shell particles embedded in the ZnO nanopillar layer (for the two lower Au-ion fluences) with increasing Au-shell thickness in correlation with the enhanced Au-implantation fluence [52]. SPR peaks resulting from Ag–Au interface in bi-metallic core-shell NPs shift rather nonlinearly with varying thickness of metal layers in core-shell NPs. Contrary, the alloy Ag–Au nanoparticles exhibited linear shift of one evidenced SPR with varying gold mole fraction [55]. The bright spots would be the biggest particles or clusters which evidenced the highest PL in the wavelength region 400 – 500 nm.

We have proved photocatalytic activity of the doped ZnO nanopillars, where Ag, Au-implanted ZnO nanopillars exhibited better preservation of the morphology for the comparable Ag+Au ion fluences implanted and simultaneously Ag+Au-ion implanted samples showed high optical absorbance in the broad wavelength range 400 – 600 nm. However, the photocatalytic properties were comparable for solely Au-implanted and Ag, Au-dually implanted ZnO nanopillars. This effect would be connected to the UV light used typically for testing which would be modified to appropriate wavelengths, where our structures exhibited more optical activity as our future task.

5. Conclusions

We have shown the possible creation of Au/Ag nanoparticles in the ZnO nanopillars by ion beam implantation with the Au-ion fluences in the range 1×10^{15} cm^{-2} to 1×10^{16} cm^{-2} and the constant Ag-ion fluence of 5×10^{15} cm^{-2} confirmed by combination of optical analytical methods (PL, DRS and SE).

As a consequence of the nanoparticle incorporation the ZnO nanopillars showed the decrease of refractive index in the nanopillar layer with embedded nanoparticles accompanied also with vertical size domain contraction with the growing Ag and Au-ion fluence identified by XRD. Internal structure and surface morphology modification is to a lesser extent exhibited in the ZnO nanopillars implanted with combination of Ag and Au ions, even the total implantation fluence is higher than for the solely Au-ion implanted samples. We concluded from our experiments that the ZnO nanopillars exhibited a promising ability to host Au, Ag NPs with SPR activity. Photocatalytic properties seem to be rather influenced by presence of nanoparticles than morphology deterioration after the implantation.

Acknowledgements

The research has been carried out at the CANAM (Centre of Accelerators and Nuclear Analytical Methods) infrastructure LM 2015056. This publication has been supported by OP RDE, MEYS, Czech Republic, under the project CANAM OP, CZ.02.1.01/0.0/0.0/16_013/0001812 and by the Czech Science Foundation (GACR No. 18-03346S). This publication has been supported by the University of J.E. Purkyne project UJEP-SGS-2021-53-002-2. The Research Council of Norway is acknowledged for the support to the Norwegian Micro- and Nano-Fabrication Facility, NorFab (project number 295864). The support from Ministry of Education, Youth and Sports (project number LM2018103) is acknowledged as well. The authors acknowledge the assistance provided by the Research Infrastructure NanoEnviCz, supported by the MEYS, Project No. LM2018124. The implantations were carried out at IBC at the Helmholtz-Zentrum Dresden - Rossendorf e. V., a member of the Helmholtz Association.

References

[1] E.N. Epie, D. Scott, W.K. Chu, Manipulating the optical properties of dual implanted Au and Zn nanoparticles in sapphire, Photonics and Nanostructures - Fundamentals and Applications 27 (2017) 17-23.

[2] G.C. Vásquez, K.M. Johansen, A. Galeckas, L. Vines, B.G. Svensson, Optical signatures of single ion tracks in ZnO, Nanoscale Adv. 2 (2020) 724–733.

[3] Z. Sofer, D. Sedmidubský, S. Huber, J. Hejtmánek, M. Maryško, K. Jurek, M. Mikulics, Flux growth of ZnO crystals doped by transition metals, Journal of Crystal Growth 314 (2011) 123–128.

[4] M. Mikulics, H. Hardtdegen, Nano-LED array fabrication suitable for future single photon lithography, Nanotechnology 26 (2015) 185302.

[5] S. Rehman, R.G. Singh, J.C. Pivin, W. Bari, F. Singh, Structural and spectroscopic modifications of nanocrystalline zinc oxide films induced by swift heavy ions, Vacuum 86 (2011) 87–90.

[6] S. Das, S. Mukhopadhyay, S. Chatterjee, P.S. Devi, G.S. Kumar, Fluorescent ZnO−Au nanocomposite as a probe for elucidating specificity in DNA interaction, ACS Omega 3 (2018) 7494−7507.

[7] V. Gerbreders, M. Krasovska, I. Mihailova, A. Ogurcovs, E. Sledevskis, A. Gerbreders, E. Tamanis, I. Kokina, I. Plaksenkova, ZnO nanostructure-based electrochemical biosensor for Trichinella DNA detection, Sensing and Bio-Sensing Research 23 (2019) 100276.

[8] D.R. Hang, S.E. Islam, K.H. Hari Sharma, S.W. Kuo, C.Z. Zhang, J.J. Wang, Annealing effects on the optical and morphological properties of ZnO nanorods on AZO substrate by using aqueous solution method at low temperature, Nanoscale Research Letters 9 (2014) 632.

[9] S. N. Das, K. J. Moon, J. P. Kar, J. H. Choi, J. Xiong, T. I. Lee, J. M. Myoung, ZnO Single Nanowire-Based UV Detectors. Appl. Phys. Lett. 97 (2) (2010) 022103.

[10] T. Chen, X. Gao, J. Zhang, J. Xu, S. Wang, Ultrasensitive ZnO Nanowire Photodetectors with a Polymer Electret Interlayer for Minimizing Dark Current. Adv. Opt. Mater. 8 (4) (2020) 1901289.

[11] C. Rodwihok, S. Choopun, P. Ruankham, A. Gardchareon, S. Phadungdhitidhada, D. Wongratanaphisan, UV Sensing Properties of ZnO Nanowires/Nanorods. Appl. Surf. Sci. 477 (2019) 159–165.

[12] S. Lu, J. Qi, S. Liu, Z. Zhang, Z. Wang, P. Lin, Q. Liao, Q. Liang, Y. Zhang, Piezotronic Interface Engineering on ZnO/Au-Based Schottky Junction for Enhanced Photoresponse of a Flexible Self-Powered UV Detector. ACS Appl. Mater. Interfaces 6 (16) (2014) 14116–14122.

[13] M. Li, M. Zhao, D. Jiang, M. Yang, Q. Li, C. Shan, X. Zhou, Y. Duan, N. Wang, J. Sun, Optimizing the Spacing of Ag Nanoparticle Layers to Enhance the Performance of ZnO/Ag/ZnO/Ag/ZnO Multilayer-Structured UV Photodetectors. Sens. Actuators Phys. 297 (2019) 111501.

[14] X. Xue, W. Zang, P. Deng, Q. Wang, L. Xing, Y. Zhang, Z. L. Wang, Piezo-Potential Enhanced Photocatalytic Degradation of Organic Dye Using ZnO Nanowires. Nano Energy *13* (2015) 414–422.

[15] L. Muñoz-Fernandez, A. Sierra-Fernandez, O. Milošević, M. E. Rabanal, Solvothermal Synthesis of Ag/ZnO and Pt/ZnO Nanocomposites and Comparison of Their Photocatalytic Behaviors on Dyes Degradation. Adv. Powder Technol. 2*7* (3) (2016) 983–993.

[16] A. Gaiardo, B. Fabbri, A. Giberti, V. Guidi, P. Bellutti, C. Malagù, M. Valt, G. Pepponi, S. Gherardi, G. Zonta, A. Martucci, M. Sturaro, N. Landini, ZnO and Au/ZnO Thin Films: Room-Temperature Chemoresistive Properties for Gas Sensing Applications. Sens. Actuators B Chem. *237* (2016) 1085–1094.

[17] T. Cesca, G. Pellegrini, V. Bello, C. Scian, P. Mazzoldi, P. Calvelli, G. Battaglin, G. Mattei, Nonlinear Optical Properties of Au–Ag Nanoplanets Made by Ion Beam Processing of Bimetallic Nanoclusters in Silica. Nucl. Instrum. Methods Phys. Res. Sect. B Beam Interact. Mater. At. 2010, 268 (19), 3227–3230.

[18] O. Peña, U. Pal, L. Rodríguez-Fernández, H. G. Silva-Pereyra, V. Rodríguez-Iglesias, J. C. Cheang-Wong, J. Arenas-Alatorre, A. Oliver, Formation of Au−Ag Core−Shell Nanostructures in Silica Matrix by Sequential Ion Implantation. J. Phys. Chem. C 113 (6) (2009) 2296–2300.

[19] Wang, Y. Enhanced Nonlinear Optical Properties of LiNbO3 Crystal Embedded with CuZn Alloy Nanoparticles by Ion Implantation. J. Alloys Compd. 2019, 8.

[20] M. Popović, M. Novaković, P. Noga, D. Vaňa, Z. Rakočević, Ion Beam Synthesis of Au-Ag Alloy Nanoparticles in TiN Thin Films. Nucl. Instrum. Methods Phys. Res. Sect. B 475 (2020) 20–27.

[21] K. H. Baik, H. Kim, S. Jang, S. Anisotropic Microstructure of Hydrothermally-Grown Non-Polar a -Plane ZnO on a -Plane GaN Film. Thin Solid Films *569* (2014) 1–5.

[22] Y. Azarov, A. Hallén, P. Rauwel, X.L. Du, A.Y. Kuznetsov, and B.G. Svensson, Effect of implanted species on thermal evolution of ion induced defects in ZnO, J. Appl. Phys. 115, (2014) 073512.

[23] A. Jagerova, P. Malinsky, R. Miksova, P. Nekvindova, J. Cajzl, S. Akhmadaliev, V. Holy, A. Mackova, Distinct defect appearance in Gd implanted polar and nonpolar ZnO surfaces in connection to ion channelling effect, JVST A 37 (2019) 061406.

[24] C. Ratajczak, P. Mieszczynski, P. Jozwik, A. Stonert, S. Prucnal, R. Heller, W. Skorupa, J. von Borany, and E. Guziewicz, Ion beam modification of ZnO epilayers: Sequential processing, Phys. Status Solidi A 215 (2018) 1700887.

[25] K.S. Ranjith, L. R. Nivedita, K. Asokan, S. Krishnamurthy, R. Pandian, M. Kamruddin, D. K. Avasthi, R. T. R. Kumar, Robust water repellent ZnO nanorod array by Swif Heavy Ion Irradiation: Efect of Electronic Excitation Induced Local Chemical State Modification, Scientific Reports 7 (2017) 3251.

[26] C. Shyamal, B. Akshaya, B. Amarabha, T. Lokesh, S. Tapobrata, A. Pushan, Applied surface science, 258 (2012) 7016-7020.

[27] V. Kondkar, D. Rukade, D. Kanjilal, V. Bhattacharyya, Controlled morphological modifications of ZnO thin films by ion irradiation, Materials Research Express 4 (2017) 116402.

[28] Jinseok Choi, and Sung Jin An, Effects of arsenic implantation and rapid thermal annealing on ZnO nanorods for *p* type doping, J. Vac. Sci. Technol. B 38 (2020) 052202.

[29] G. Perillat-Merceroz, F. Donatini, R. Thierry, P-H. Jouneau, P. Ferret, et al. Structural recovery f ion implanted ZnO nanowires. Journal of Applied Physics, American Institute of Physics 111 (8) (2012) 083524

[30] A. Mackova, P. Malinsky, A. Jagerova, R. Miksova, O. Lalik, P. Nekvindova, J. Mistrik, P. Marvan, Z. Sofer, V. Holy, J. D. Schutter, U. Kentsch, A. Azarov, A. Galeckas, Energetic Au ion beam implantation of ZnO nanopillars for optical response modulation, J. Phys. D: Appl. Phys. 55 (2022) 215101.

[31] C. F. Dee, I. Ahmad, L. Yan, X. Zhou, B. Y. Majlis, Amorphization of ZnO Nanowires By Proton Beam Irradiation, Nano 6 (2011) 259–263.

[32] J. Cajzl, K. Jeníčková, P. Nekvindová, A. Michalcová, M. Veselý , A. Macková, P. Malinský, A. Jágerová, R. Mikšová, S. Akhmadaliev, Creation of gold nanoparticles in ZnO by ion implantation–DFT and experimental studies, Nanomaterials 10 (2020) 2392.

[33] R. Viter, Z. Balevicius, A. Abou Chaaya, I. Baleviciute, S. Tumenas, L. Mikoliunaite, A. Ramanavicius, Z. Gertnere, A. Zaleska, V. Vataman, V. Smyntyna, D. Erts, P. Mielee and M. Bechelany, The influence of localized plasmons on the optical properties of Au/ZnO nanostructures, J. Mater. Chem. C 3 (2015) 6815

[34] W.K. Tana, T. Itob, G. Kawamurab, H. Mutoc, Z. Lockmand, A. Matsuda, Controlled facile fabrication of plasmonic enhanced Au-decorated ZnO nanowire arrays dye-sensitized solar cells, Materials Today Communications 13 (2017) 354–358.

[35] X. Qu, R. Yang, F. Ton, Y. Zhao, M. H. Wang, Hierarchical ZnO microstructures decorated with Au nanoparticles for enhanced gas sensing and photocatalytic properties. Powder Technol. 330 (2018) 259–265.

[36] T. Bora, P. Sathe, K. Laxman, S. Dobretsov, J. Dutt, Defect engineered visible light active ZnO nanorods for photocatalytic treatment of water. Catal Today 248 (2017) 1–18.

[37] Y.I. Alivov, Ü. Özgür, S. Dogan, D. Johnstone, V. Avrutin, N. Onojima, C. Liu, J. Xie, Q. Fan, H. Morkoç, Photoresponse of n-ZnO/p-SiC heterojunction diodes grown by plasma-assisted molecular-beam epitaxy. Appl Phys Lett . 86 (2005) 241108.

[38] J. Mistrik, S. Kasap, H.E. Ruda, C. Koughia, and J. Singh, Optical pProperties of Electronic Materials: Fundamentals and Characterization, in: S. Kasap and P. Capper (Eds.), Springer Handbook of Electronic and Photonic Materials, 2nd ed., Springer International Publishing, Berlin, Heidelberg, 2017, Chap. 3, pp. 47–84.

[39] Ziegler, J. F.; Ziegler, M. D.; Biersack, J. P. SRIM – The Stopping and Range of Ions in Matter (2010). Nucl. Instrum. Methods Phys. Res. Sect. B, 268 (2010) 1818–1823.

[40] A. Mackova, A. Jagerova, P. Malinsky, M. Cutroneo, J. Flaks, P. Nekvindova, A. Michalcova, V. Holy, T. Kosutova, Nanostructures in various Au ion-implanted ZnO facets modified using energetic O ions**,** Physical Chemistry Chemical Physics 22 (41) (2020) 23563–235737.

[41] M. Mayer, P. Malinsky, F. Schiettekatte, Z. Zolnai, Intercomparison of ion beam analysis software for the simulation of backscattering spectra from two-dimensional structures, Nuclear Instruments and Methods in Physics Research B 385 (2016) 65–73.

[42] P. Malinsky, V. Hnatowicz, A. Mackova, Computer simulation of RBS spectra from samples with surface roughness, Nuclear Instruments and Methods in Physics Research B 371 (2016) 101–105.

[43] T. Ungár, J. Gubicza, G. Ribárik, and A. Borbély, Crystallite size distribution and dislocation structure determined by diffraction profile analysis: principles and practical application to cubic and hexagonal crystals, J. Appl. Cryst. 34 (2001) 298–310.

[44] A . Macková, P. Malinský, A. Jagerová, R. Mikšová, Z. Sofer, K. Klímová, M. Mikulics, R. Böttger, S. Akhmadaliev, J. Oswald, Damage accumulation and implanted Gd and Au position in a- and c-plane, GaN, Thin Solid Films 680 (2019) 102–113.

[45] A. Azarov, A. Galeckas, V. Venkatachalapathy, Zengxia Mei, Xiaolong Du, E. Monakhov, A. Kuznetsov, Acceptor complex signatures in oxygen-rich ZnO thin films implanted with chlorine ions, J. Appl. Phys. 128 (2020) 125701

[46] M. Rycenga, C. M. Cobley, Jie Zeng, Weiyang Li, C. H. Moran, Q. Zhang, D. Qin, Y. Xia, Controlling the Synthesis and Assembly of Silver Nanostructures for Plasmonic Applications, Chem. Rev. 111 (2011) 3669–3712.

[47] S. Link, M. A. El-Sayed, Shape and size dependence of radiative, non-radiative and photothermal properties of gold nanocrystals, Int. Rev. Phys. Chem. 19 (2000) 409.

[48] F. Wang and Y.R. Shen, General Properties of Local Plasmons in Metal Nanostructures, Phys. Rev. Lett. 97 (2006) 206806.

[49] T. Wu, A. Wang, Li Zheng, G. Wang, Q. Tu, B. Lv, Z. Liu, Z. Wu, Y. Wang, Evolution of native defects in ZnO nanorods irradiated with hydrogen ion, Scientific Reports 9 (2019) 17393.

[50] N. K. R. Eswar, P. Ch. Ramamurthy and G. Madras, Enhanced sunlight photocatalytic activity of Ag_3PO_4 decorated novel combustion synthesis derived TiO_2 nanobelts for dye and bacterial degradation, Photochem. Photobiol. Sci., 14 (2015) 1227.

[51] N.U. Alvi, S. Hussain, J. Jensen, O. Nur, M. Willander, Influence of helium-ion bombardment on the optical properties of ZnO nanorods/p-GaN light-emitting diodes, Nanoscale Res Lett. 6 (2011) 628.

[52] S. W. Verbruggen, M. Keulemans, J. A. Martens, S. Lenaerts, Predicting the surface plasmon resonance wavelength of gold–silver alloy nanoparticles, J. Phys. Chem. C 117 (2013) 19142–19145.

[53] S. Wolf, J. Rensberg, A. Johannes, R. Thomae, F. Smit, R. Neveling, M. Moodley, T. Bierschenk, M. Rodriguez, B. Afra, S. B. Hasan, C. Rockstuhl, M. Ridgway, K. Bharuth-Ram, C. Ronning, Shape manipulation of ion irradiated Ag nanoparticles embedded in lithium niobate, Nanotechnology 27 (2016) 145202.

[54] H. Yu, Y. Peng, Y. Yang, Zhi-Yuan Li, Plasmon-enhanced light–matter interactions and applications, Computational Materials, 5 (2019) 45.

[55] A. Alqudami, S. Annapoorni, S.M. Shivaprasad, Ag–Au alloy nanoparticles prepared by electro-exploding wire technique, J. Nanopart. Res. 10 (2008) 1027.